DOI: 10.1002/((please add manuscript number))
Article type: Communication

Infrared solution-processed quantum dot solar cells reaching external quantum efficiency of 80% at 1.35 μm and J_{sc} in excess of 34 mA/cm^2

*Yu Bi[1†], Santanu Pradhan[1†], Shuchi Gupta[1], Zafer Akgul[1], Alexandros Stavrinadis[1], and Gerasimos Konstantatos[1, 2]**

1. ICFO—Institut de Ciencies Fotoniques, The Barcelona Institute of Science and Technology, Av. Carl Friedrich Gauss, 3, 08860 Castelldefels (Barcelona), Spain
2. ICREA—Institució Catalana de Recerca i Estudis Avançats, Passeig Lluís Companys 23, 08010 Barcelona, Spain

***E-mail:** Gerasimos.Konstantatos@icfo.eu

Keywords: Short-wave infrared, PbS, Colloidal Quantum dots, Solar cells,

Developing low-cost photovoltaic absorbers that can harvest the short-wave infrared (SWIR) part of the solar spectrum, which remains unharnessed by current Si-based and perovskite photovoltaic technologies, is a prerequisite for making high efficiency, low-cost tandem solar cells. Here we report infrared PbS colloidal quantum dot (CQD) solar cells employing a hybrid inorganic-organic ligand exchange process that result in an external quantum efficiency of 80% at 1.35 μm, leading to a short circuit current density of 34 mA/cm^2 and power conversion efficiency (PCE) up to 7.9 %, which is a current record for SWIR CQD solar cells. When this cell is placed at the back of a $MAPbI_3$ perovskite film, it delivers an extra 3.3% PCE by harnessing light beyond 750 nm.

Colloidal quantum dots (CQD) have been extensively studied as a third generation solar cell technology. [1-5] PbS CQD with a wide bandgap tuning range could be used for harvesting the near and short-wave infrared (SWIR) part of the solar spectrum, at which silicon and perovskite solar cells are transparent. Recently, efforts have been focused on perovskite or Si based tandem solar cells, as means to surpass Si efficiency records and reduce the per Watt cost of PV systems. [6-9] A theoretical power conversion efficiency (PCE) up to 42% is predicted in a tandem solar cell comprising two current matched subcells with bandgaps of 1.6 eV and 0.95 eV respectively, which is substantially higher than the 31% single junction limit. [10, 11] While an abundance of materials can potentially serve as the 1.6 eV absorber in tandem solar cells, the same is not true for the 0.95 eV one. Hence, here we focus on developing the lower bandgap subcell. PbS CQD with tuneable bandgap (0.7-2.1 eV) makes an excellent choice in view of their low cost, solution processability and bandgap tunability,[12] especially PbS QD with a first exciton peak around 1.3 μm (0.95eV), which have been proposed to complement ideally with lead halide perovskites in tandem solar cells.[13] The efficiencies of PbS QD single junction solar cells have improved substantially up to 11.6 %, thanks to advances in device structure optimization and surface passivation strategies.[14, 15] These have been achieved with CQDs whose bandgap are around 1.3-1.4 eV. However, little attention has been given to lower bandgap (< 1eV) PbS solar cells. In the past, a 7.3% efficiency has been reported from 1 eV bandgap PbS QDs solar cells [13] Air-stable 1.3 μm PbS solar cells based on a novel one-step fabrication process have also been reported, yet their PCE was 3.5%. [16]

Overall, in order to achieve highly efficient and stable PbS QD solar cells beyond 1100 nm, several issues need to be tackled; for example, (i) New strategies applied for the surface passivation on large PbS QDs, that serve not only to minimize the surface trap density but also to favourably tune the band levels of the QD film to facilitate efficient electron injection in the electron acceptor layer.[17, 18] (ii) Band alignment engineering should be reconsidered for the

purpose of optimizing the contacts of the PbS QDs active layer. The energy levels of QDs shift with their size. [19] Thus for the 1.3 μm PbS QDs active layer, an electron-accepting layer with deeper conduction band level may be needed instead of the usual ZnO and TiO_2 layers. [16, 20] (iii) The stability of the large PbS QDs solar cells needs to be studied and improved. PbS QD solar cells with different size QDs have been reported with a large variation on their stability. [17, 21] Specifically, the air stability of the cells has shown an abrupt transition to the worse when crossing a diameter of 4 nm in PbS QDs. [21] Having these issues in mind, here we report a low temperature synthesis of stable 1.3-1.4 μm PbS QDs by using a multi-injection method. A hybrid inorganic-organic ligand treatment combining zinc iodide (ZnI_2) and 3-mercaptapropionic acid (MPA) has been used to surface passivate the as-obtained PbS QDs. In addition, a thin layer of Aluminium doped ZnO (AZO) deposited via sputtering was introduced as the electron-accepting layer of the solar cell. As a result, an external quantum efficiency (EQE) up to 80% at the first exciton peak around 1.35 μm has been achieved in these devices, resulting in a short circuit current density (J_{SC}) of 34 mA/cm^2 and PCE of 7.9%.

For the synthesis of 1.35 μm bandgap PbS QDs, instead of using one of the recipes available in the literature, [22-26] we have followed a low temperature synthetic approach by using a multi-injection method with minor modifications. [26] (The detailed synthesis procedures can be found in the experimental section) Absorption spectra, TEM image and the size distribution histogram of the as-obtained PbS QDs are shown in the **Figure S1**. In **Figure 1a**, a cross-sectional FIB SEM image of the PbS QD solar cell is presented. 30 nm of AZO sputtered on top of cleaned ITO substrate was used as the electron-accepting layer, followed by the layer-by-layer deposition method for PbS QDs film. An additional thin 1,2-ethanedithiol (EDT) treated PbS QD film was deposited atop as the electron-blocking layer with a thickness of 40 nm. In the end, the device was completed by depositing 80 nm of Au as the back electrode. (The detailed

device fabrication process can be found in the experimental section). The most critical determinant factor for high performance is the selection of an appropriate passivation scheme. It serves to minimize recombination, increase carrier transport and tune the band levels of the PbS QD film favourably for charge extraction. In identifying the optimal ligand chemistry, we focused on two strategies that we reported previously in near infrared (NIR) PbS QD solar cells with exciton peak at 950 nm. [4, 27] One is based on a pure halide passivation employing 1-ethyl-3-methylimidazolium iodide (EMII) as the halide precursor ligand, whereas the second was based on a hybrid organic-inorganic mixed ligand strategy using ZnI_2_MPA. We hypothesized that the mixed ligand strategy would serve better, since it would not downshift the energy levels of large PbS QDs to the extent that pure halide passivation has been reported to do. [12] The device performance of the EMII and ZnI_2_MPA treated solar cells are summarized in **Table 1**. The ZnI_2_MPA treated device significantly outperforms the EMII treated one (PCE of 6.7 % and 1.1%, respectively). The EMII treated device suffers from inefficient charge extraction as evidenced by the extremely low J_{SC} (11.77 mA/cm^2). To account for this, we sought the origin in the band levels of these two PbS QD films employing UV photoelectron spectroscopy (UPS). The comparison of the UPS data between EMII and ZnI_2_MPA treated PbS QD films is shown in **Figure S2**. ZnI_2_MPA treated PbS QD films possess shallower conduction band compared to the EMII counterpart, thus forming a favourable electron accepting junction with AZO. Hence, with an additional EDT treated PbS layer (shown in **Figure 1b**) as the efficient electron-blocking layer, ZnI_2_MPA treated PbS QDs film results in an efficient QD solar cell. AZO was selected instead of ZnO in order to facilitate a more favourable electron accepting band offset when in contact with the SWIR PbS QD film (Fig. 1b). Devices based on ZnO nanocrystals (NCs) have also been fabricated and tested as shown in **Table S1**, they are outperformed by the ones based on AZO.

Device performance of the SWIR PbS QD solar cells was further optimized by performing a thickness dependence study. A thickness of 420 nm for the active layer has led to the best

performing devices (**Table S2**). Current density –voltage (J-V) curves of the optimized device with forward and reversed scans are shown in **Figure 1c**. The highest J_{SC} of 34 mA/cm^2 was measured, leading to a PCE of 7.9%. In addition, negligible J-V hysteresis loss was observed in this device. The Inset plot in **Figure 1c** shows the simulated J_{SC} as a function of the active layer thickness (100-600 nm) by using the transfer matrix method (TMM), [28-30] while keeping other layer thicknesses intact. The optical modelling yields a J_{SC} of 35 mA/cm^2 for a thickness of 420-440 nm in very good agreement with the experimental data. **Figure 1d** illustrates the experimentally measured and optically simulated EQE spectra of the best performing 420-nm-thick device, being in very good agreement. The origin of the record J_{SC} stems from an average EQE of 90% in the visible region of 400nm to 700nm, and a remarkably high EQE (~80%) in the first exciton peak region (1.3 to 1.4 μm). This demonstrates a broad efficient spectral response with an integrated J_{SC} of 33.8 and 34.6 mA/cm^2 respectively in measured and simulated EQE, which is consistent with the high J_{SC} observed in the J-V measurements under AM1.5 condition. It is noteworthy that TMM simulated J_{SC} and EQE values rely solely on optical modelling, which ignores carrier transport and collection losses. The agreement of the optical simulations with the experimental data indicates that the ZnI_2_MPA treated 1.35 μm PbS QD films are well passivated, and thus lead to a near unity charge collection efficiency despite having a 420 nm thick QD absorber.

To account for this remarkable device performance, different optoelectronic characterization techniques have been employed that provide insights about the charge generation, transport and recombination dynamics within the device. **Figure 2a** shows the $1/C^2$ – V plot for standard Mott-Schottky analysis. The fitting of the linear region gives the value of build-in potential (V_{bi}) as 0.47 V. This is consistent with the V_{OC} we have achieved and the positions of the energy level for these PbS QDs considering the cells suffer from the in-gap trap induced V_{OC} deficit. The calculated depletion width (W_D) at zero bias from the plot was found to be 265 nm, which

is substantially larger than the ones reported in standard NIR PbS CQD solar cells with an exciton peak at 950 nm. [31-33] The large W_D constitutes the first determinant factor of near unity charge collection efficiency achieved in such a thick device. To identify the second determinant factor, the carrier diffusion length, we employed transient photovoltage (TPV) and photo-current (TPC) measurements as they can further enlighten the recombination dynamics in the device. **Figure 2b** shows the dependence of carrier lifetime **τ** (measured through TPV) and the in-gap trap density (obtained with the combination of TPC and TPV techniques) with device V_{OC}. These values are very similar to the ones reported for NIR PbS QD based devices. [34] The carrier mobility in the device was found to be on the order of 0.02 cm^2/Vs through time-of-flight measurements. (See Supporting Information **Figure S3**) To estimate the carrier diffusion length (L_D), we used the formula: $L_D = \sqrt{D\tau}$ (where D is the diffusivity and τ is the carrier lifetime). By using Einstein's relation, we can rewrite it as, $L_D = \sqrt{\frac{\mu(kT)\tau}{q}}$ (where μ is mobility, kT is thermal energy and q is elementary charge). The caculated L_D is 273 nm by plugging in the values we acquired from the corresponding measurements. (μ of 0.018 $cm^2V^{-1}s^{-1}$ and τ of 1.6 μs: from TPV at 1 sun) Taken the sum of depletion width and diffusion length yields a thickness of 538 nm, in which photogenerated carriers can be efficiently extracted from the device with minimal losses. This accounts for the near unity charge collection efficiency achieved in the optically optimized 420 nm thick solar cell.

In **Figure 2c** we plot the recombination rate (R), defined as the ratio of the photogenerated charge carriers (n) over **τ**, as a function of carrier density *n*. R shows a near 2nd order dependence ($R \propto n^p, p{\sim}1.9$), suggestive of free carrier recombination as the dominant recombination process with some limited involvement of traps in the recombination dynamics. (A value close to unity points to free-to-bound charge recombination through traps and a value greater than two indicates Auger recombination. [35]) Intensity dependent V_{OC} and photocurrent (J_{ph})

measurements give additional insights about the charge generation and recombination mechanisms in the device. **Figure 2d** shows the variation of V_{OC} and J_{ph} with the intensity of incident light. The J_{ph} shows a near unity intensity dependence ($J_{ph} \propto \Phi^m$, Φ is intensity, m = 0.98) indicative of generation limited photocurrent. V_{OC} intensity dependence follows the relation, $V_{OC} \sim \frac{\eta kT}{q} \ln(\Phi)$, where kT is the thermal energy, q is the elementary charge, and $\boldsymbol{\eta}$ is the diode ideality factor. The value of $\boldsymbol{\eta}$ obtained is 1.41, which points to the presence of trap assisted recombination, yet it is still better than most of the halide treated NIR PbS based devices, reported between 1.5 and 1.8. [33, 36, 37] Based on these findings, we conclude that with the hybrid ZnI_2_MPA ligand treatment we preserve, to a large extent, the solar grade quality in large PbS QDs with exciton peak at 1350 nm. It allows us to develop high efficiency infrared solar cells.

To assess the potential of this device to act as a subcell in combination with other established PV technologies that can harness more efficiently the visible and NIR part of solar spectrum, we have measured the performance of the SWIR PbS QD solar cell by using a methylammonium lead iodide ($MAPbI_3$) perovskite filter (long pass 750 nm) or a silicon filter (1100 nm long pass) between the device and the AM1.5 solar simulator. The device performance of the SWIR cells with and without optical filtering is summarized in **Table 2**. The PCE is 3.33% when using a $MAPbI_3$ perovskite thin film of 350 nm in thickness and a bandgap of 1.6 eV. Figure 3 illustrates the J-V characteristics and the corresponding EQE spectra of the SWIR PbS QD solar cell in the presence and absence of the perovskite thin film in front. Even when a silicon wafer is placed in front of the cell the PCE is 0.67 % thanks to the extended absorption range in the SWIR that can be harnessed up to 1400 nm.

Besides high J_{SC} and PCE, device stability is another key parameter for solar cells. [38, 39] In the past, the stability of such devices was found to be poor when only MPA was used for the ligand exchange treatment. [40, 41] In our case, to perform preliminary photostability studies, we

exposed non-encapsulated devices in ambient air conditions, continuously under AM1.5 solar illumination while performing J-V measurements. The evolution of the device performance as a function of time is shown in the **Figure 4a**. Device performance improves slightly at the beginning likely due to the light soaking of AZO layer, stabilizing later at the maximum value and remaining unchanged over 5 hours of continuous AM 1.5 illumination. To further demonstrate the stability of the devices, their performance was monitored during 90 days as a long term stability test shown in **Figure 4b**. J_{SC} improves with time, while V_{OC} and FF remain constant for the first 30 days, leading to slightly improved PCE from 7.5% to 7.9%. Subsequently, J_{SC} further increases up to 36 mA/cm^2, yet V_{OC} and FF decrease, resulting in a PCE of 7.5% after 90 days. Overall the solar cell performance remains the same after 90 days of storage.

Experimental Section

PbS Quantum Dots synthesis: 1.35 μm PbS QDs are synthesized via a reported multi-injection method with minor modification. Typically, PbO (0.45g) was dissolved in a mixture of ODE (50ml) and oleic acid (3.8ml) at 95 °C. under vacuum for 12h. The temperature was adjusted to 80 °C. Different amounts of Hexamethyldisilathiane (TMS) (60μl for the first injection and 25 μl for the additional 3 injections) were dissolved in ODE (3ml). The solution of 60μl TMS was injected into the lead precursor solution at 80 °C, the additional 3 injections were sequentially followed every fixed time. When the injection finished, the flask was allowed to gradually cool down to room temperature under stirring. QDs were purified in air by adding acetone, followed by centrifugation. The final QDs were dispersed in toluene with a concentration of 40mg/ml for the solar cell fabrication.

Fabrication of solar cells: ITO substrates were cleaned thoroughly in the soap water, water, acetone and isopropanol respectively in ultrasonic bath. Al doped ZnO (AZO) was deposited on the top of the clean ITO substrates by an RC magnetron sputtering (AJA Orion 8 HV) at the room temperature. The 30nm AZO was sputtered in an Ar/O2 mixture (flux ratio of 18:2) at a pressure of 1.4 mTorr at a rate of 0.3 $ÅS^{-1}$. PbS layer was deposited by a layer-by-layer spin coating method. PbS QDs with concentration of 30 g/L covered the whole substrate, followed by spinning at 2500 rpm for 20s. ZnI_2/MPA ($25X10^{-3}$ M with 0.01% MPA in methanol) solution covered the PbS layer for 5 s before spinning at 2500 rpm for 10 s. The spinning substrate was flushed twice by few drops of methanol and spun for 20 s to make film dry. The above process was repeated till desired thickness achieved. The final two layers PbS were treated with 0.02% V/V EDT. The PbS film was covered by EDT acetonitrile solution for 30 s before spun at 2500 rpm for 10 s. The spinning substrate was flushed by 10 drops of acetonitrile followed by spinning for 20 s to make film dry. The above process was repeated twice to obtain EDT-treated PbS QD layer. All the active layer fabrication process was carried out in a fume hood in ambient.

100nm Au was deposited on the films by thermal evaporation at a speed of 1 Å s-1 by using a Kurt J. Lesker Nano 36 system at a base pressure lower than 10 $^{-6}$mbar. The solar cells were transferred from the evaporator and transferred into the glove box for annealing at 80 C for 5 min. The active area of the device is 0.0314 cm^2. All the devices were taken out of the glovebox and stored in the air for the further characterizations.

J-V characterizations: All the devices were characterized in the air under ambient conditions. The current density – voltage measurements were carried out using a Keithley 2400 source under AM1.5 illuminations (Oriel sol 3A, Newport Corporation). The accuracy of the measurements was determined as ±4%. For photostability test, the J-V measurements were performed from time to time on the solar cells, which were continuously exposed to the AM1.5 illumination in the air.

EQE measurements: EQE spectra were recorded with a lock-in amplifier (Stanford Research System SR830) under chopped monochromatic light generated by white light source from a xenon lamp passing through a Newport Cornerstone 260 monochromator. The output power was corrected with Newport 818-UV and Newport 838-IR photodetectors.

UPS characterization: UPS measurements were performed with a SPECS PHOIBOS 150 hemispherical analyzer (SPECS GmbH, Berlin, Germany) in ultra-high vacuum conditions (10–10 mbar). UPS measurements with monochromatic HeI UV source (21.2 eV).

C-V measurement: The Capacitance-Voltage (C-V) measurement was performed with Agilent B1500A semiconductor analyzer measurement unit. The AC bias voltage amplitude was set at 50 mV with frequency 1 kHz. The acquired C-V data was processed with Mott-Schottky analysis for determining built-in potential and charge density and depletion width.

Intensity dependent J_{ph} and V_{OC} measurement: The intensity dependent J_{ph} and V_{OC} was performed with Keithley 2400 source meter. The Illumination intensity of AM 1.5 was maintained using a class AAA solar simulator (Oriel sol3A, Newport Corporation). The intensity of the light source is calibrated with a standard Si solar cell provided by Fraunhofer

ISE with mentioned mismatch factor of 1.0063. The intensity was varied using neutral density filters from .01 sun to 1 sun.

Transient photovoltage and photo-current measurements: Transient photovoltage (TPV) and photocurrent (TPC) of the devices were measured with an in-house-built set-up. The set-up comprises a LED lamp to provide steady state white bias light, a 637 nm wavelength laser (Vortran Stradus-637) and an Agilent 4000X oscilloscope. The LED lamp was used to get steady V_{OC} of the device. The intensity of the lamp was controlled by the external applied DC bias and was reduced with metal-mesh filters according to the necessity. The laser was controlled by the function generator of the oscillator with a frequency of 10 Hz and pulse width of 100 μs. The intensity of the laser was precisely controlled to keep the voltage transient amplitude under 5% of the steady state light bias. The oscilloscope records the data using 1 MΩ input impedance for the TPV measurement and 50 Ω for TPC measurement. The V_{OC} decay curves were fitted with exponential decay to find the recombination time. The TPC curve was integrated to get the charge generated (ΔQ) in the devices due to the laser pulse. The capacitance (C) was calculated from the $C= \Delta Q/\Delta V_{OC}$ relation. The total charge carrier was calculated from the integration of C vs V_{OC} plot. Charge carrier density (n) was calculated by dividing the total charge carriers with the device volume. The density of the trap states were calculated by taking the derivative of the charge density with respect to the V_{OC} following a previously reported procedure.[42]

Supporting Information
Supporting Information is available from the Wiley Online Library or from the author.

Acknowledgements
We acknowledge financial support from the European Research Council (ERC) under the European Union's Horizon 2020 research and innovation programme (grant agreement No 725165), the Spanish Ministry of Economy and Competitiveness (MINECO) and the "Fondo Europeo de Desarrollo Regional" (FEDER) through grant MAT2014-56210-R. This work was also supported by AGAUR under the SGR grant (2014SGR1548) and by European Union H2020 Programme under grant agreement n°696656 Graphene Flagship. We also acknowledge financial support from Fundacio Privada Cellex, the CERCA Programme and the Spanish Ministry of Economy and Competitiveness, through the "Severo Ochoa" Programme for Centres of Excellence in R&D (SEV-2015-0522). We are also thankful to Dr. Q. Liu for providing us with a perovskite thin film layer. Dr. Y. Bi and Dr. S. Pradhan contributed equally to this work.

Received: ((will be filled in by the editorial staff))
Revised: ((will be filled in by the editorial staff))
Published online: ((will be filled in by the editorial staff))

References

[1] C-H. M. Chuang, P. R. Brown, V. Bulović, M. G. Bawendi, *Nat. Mater.* **2014**, *13*, 796.

[2] X. Lan, O. Voznyy, F. P. Garcia de Arquer, M. Liu, J. Xu, A. H. Proppe, G. Walters, F. Fan, H. Tan, M. Liu, Z. Yang, S. Hoogland, E. H. Sargent, *Nano Lett.* **2016**, *16*, 4630.

[3] M. Liu, F. P. de Arquer, Y. Li, X. Lan, G. H. Kim, O. Voznyy, L. K. Jagadamma, A. S. Abbas, S. Hoogland, Z. Lu, J. Y. Kim, A. Amassian, E. H. Sargent, *Adv. Mater.* **2016**, *28*, 4142.

[4] Y. Cao, A. Stavrinadis, T. Lasanta, D. So, G. Konstantatos, *Nat. Energy* **2016**, *1*, 16035.

[5] G. H. Carey, A. L. Abdelhady, Z. Ning, S. M. Thon, O. M. Bakr, E. H. Sargent, *Chem. Rev.* **2015**, *115*, 12732.

[6] K. A. Bush, A. F. Palmstrom, Z. J. Yu, M. Boccard, R. Cheacharoen, J. P. Mailoa, D. P. McMeekin, R. L. Z. Hoye, C. D. Bailie, T. Leijtens, I. M. Peters, M. C. Minichetti, N. Rolston, R. Prasanna, S. Sofia, D. Harwood, W. Ma, F. Moghadam, H. J. Snaith, T. Buonassisi, Z. C. Holman, S. F. Bent, M. D. McGehee, *Nat. Energy* **2017**, *2*, 17009.

[7] A. Guchhait, H. A. Dewi, S. W. Leow, H. Wang, G. Han, F. B. Suhaimi, S. Mhaisalkar, L. H. Wong, N. Mathews, *ACS Energy Lett.* **2017**, *2*, 807.

[8] T. Todorov, O. Gunawan, S. Guha, *Mol. Syst. D & E.* **2016**, *1*, 370.

[9] G. E. Eperon, T. Leijtens, K. A. Bush, R. Prasanna, T. Green, J. T.-W. Wang, D. P. McMeekin, G. Volonakis, R. L. Milot, R. May, A. Palmstrom, D. J. Slotcavage, R. A. Belisle, J. B. Patel, E. S. Parrott, R. J. Sutton, W. Ma, F. Moghadam, B. Conings, A. Babayigit, H.-G. Boyen, S. Bent, F. Giustino, L. M. Herz, M. B. Johnston, M. D. McGehee, H. J. Snaith, *Science* **2016**, *354*, 861.

[10] A. D. Vos, *J. Phys. D: Appl. Phys.* **1980**, *13*, 839.

[11] W. Shockley, H. J. Queisser, *J. Appl. Phys.* **1961**, *32*, 510.

[12] P. R. Brown, D. Kim, R. R. Lunt, N. Zhao, M. G. Bawendi, J. C. Grossman, V. Bulović, *ACS Nano.* **2014**, *8*, 5863.

[13] A. H. Ip, A. Kiani, I. J. Kramer, O. Voznyy, H. F. Movahed, L. Levina, M. M. Adachi, S. Hoogland, E. H. Sargent, *ACS Nano* **2015**, *9*, 8833.

[14] J. Choi, Y. Kim, J. W. Jo, J. Kim, B. Sun, G. Walters, F. P. García de Arquer, R. Quintero-Bermudez, Y. Li, C. S. Tan, L. N. Quan, A. P. T. Kam, S. Hoogland, Z. Lu, O. Voznyy, E. H. Sargent, *Adv. Mater.* **2017**, *29*, 1702350.

[15] M. Liu, O. Voznyy, R. Sabatini, F. P. Garcia de Arquer, R. Munir, A. H. Balawi, X. Lan, F. Fan, G. Walters, A. R. Kirmani, S. Hoogland, F. Laquai, A. Amassian, E. H. Sargent, *Nat. Mater.* **2017**, *16*, 258.

[16] A. Kiani, B. R. Sutherland, Y. Kim, O. Ouellette, L. Levina, G. Walters, C.-T. Dinh, M. Liu, O. Voznyy, X. Lan, A. J. Labelle, A. H. Ip, A. Proppe, G. H. Ahmed, O. F. Mohammed, S. Hoogland, E. H. Sargent, *Appl. Phys. Lett.* **2016**, *109*, 183105.

[17] H. Choi, J.-H. Ko, Y.-H. Kim, S. Jeong, *J. Am. Chem. Soc.* **2013**, *135*, 5278.

[18] D. N. Dirin, S. Dreyfuss, M. I. Bodnarchuk, G. Nedelcu, P. Papagiorgis, G. Itskos, M. V. Kovalenko, *J. Am. Chem. Soc.* **2014**, *136*, 6550.

[19] J. Jasieniak, M. Califano, S. E. Watkins, *ACS Nano* **2011**, *5*, 5888.

[20] J. Gao, J. M. Luther, O. E. Semonin, R. J. Ellingson, A. J. Nozik, M. C. Beard, *Nano Lett.* **2011**, *11*, 1002.

[21] D. Zherebetskyy, M. Scheele, Y. Zhang, N. Bronstein, C. Thompson, D. Britt, M. Salmeron, P. Alivisatos, L.-W. Wang, *Science* **2014**, *344*, 1380.

[22] J. J. Choi, W. N. Wenger, R. S. Hoffman, Y. F. Lim, J. Luria, J. Jasieniak, J. A. Marohn, T. Hanrath, *Adv. Mater.* **2011**, *23*, 3144.

[23] X. Wang, G. I. Koleilat, J. Tang, H. Liu, I. J. Kramer, R. Debnath, L. Brzozowski, D. A. R. Barkhouse, L. Levina, S. Hoogland, E. H. Sargent, *Nat. Photonics* **2011**, *5*, 480.

[24] B. Hou, Y. Cho, B. S. Kim, J. Hong, J. B. Park, S. J. Ahn, J. I. Sohn, S. Cha, J. M. Kim, *ACS Energy Lett.* **2016**, *1*, 834.

[25] E. M. Miller, D. M. Kroupa, J. Zhang, P. Schulz, A. R. Marshall, A. Kahn, S. Lany, J. M. Luther, M. C. Beard, C. L. Perkins, J. van de Lagemaat, *ACS Nano* **2016**, *10*, 3302.

[26] J. W. Lee, D. Y. Kim, S. Baek, H. Yu, F. So, *Small* **2016**, *12*, 1328.

[27] S. Pradhan, A. Stavrinadis, S. Gupta, Y. Bi, F. Di Stasio, G. Konstantatos, *Small* **2017**, *13*, 1700598.

[28] G. F. Burkhard, E. T. Hoke, M. D. McGehee, *Adv. Mater.* **2010**, *22*, 3293.

[29] E. Centurioni, *Appl. Opt.* **2005**, *44*, 7532.

[30] L. A. A. Pettersson, L. S. Roman, O. Inganäs, *J. Appl. Phys.* **1999**, *86*, 487.

[31] X. Lan, O. Voznyy, A. Kiani, F. P. García de Arquer, A. S. Abbas, G.-H. Kim, M. Liu, Z. Yang, G. Walters, J. Xu, M. Yuan, Z. Ning, F. Fan, P. Kanjanaboos, I. Kramer, D. Zhitomirsky, P. Lee, A. Perelgut, S. Hoogland, E. H. Sargent, *Adv. Mater.* **2016**, *28*, 299.

[32] A. Stavrinadis, A. K. Rath, F. P. G. de Arquer, S. L. Diedenhofen, C. Magén, L. Martinez, D. So, G. Konstantatos, *Nat. Commun.* **2013**, *4*, 2981.

[33] M. J. Speirs, D. N. Dirin, M. Abdu-Aguye, D. M. Balazs, M. V. Kovalenko, M. A. Loi, *Energy Environ. Sci.* **2016**, *9*, 2916.

[34] A. Stavrinadis, S. Pradhan, P. Papagiorgis, G. Itskos, G. Konstantatos, *ACS Energy Lett.* **2017**, *2*, 739.

[35] T. Kirchartz, J. Nelson, *Phys. Rev. B* **2012**, *86*, 165201.

[36] C.-H. M. Chuang, A. Maurano, R. E. Brandt, G. W. Hwang, J. Jean, T. Buonassisi, V. Bulović, M. G. Bawendi, *Nano Lett.* **2015**, *15*, 3286.

[37] P. R. Brown, R. R. Lunt, N. Zhao, T. P. Osedach, D. D. Wanger, L.-Y. Chang, M. G. Bawendi, V. Bulović, *Nano Lett.* **2011**, *11*, 2955.

[38] L. Tan, P. Li, B. Sun, M. Chaker, D. Ma, *ACS Energy Lett.* **2017**, *2*, 1573.

[39] R. Azmi, S. Sinaga, H. Aqoma, G. Seo, T. K. Ahn, M. Park, S.-Y. Ju, J.-W. Lee, T.-W. Kim, S.-H. Oh, S.-Y. Jang, *Nano Energy* **2017**, *39*, 86.

[40] L.-H. Lai, L. Protesescu, M. V. Kovalenko, M. A. Loi, *Phys. Chem. Chem.* **2014**, *16*, 736.

[41] A. H. Ip, A. J. Labelle, E. H. Sargent, *Appl. Phys. Lett.* **2013**, *103*, 263905.

[42] A. H. Ip, S. M. Thon, S. Hoogland, O. Voznyy, D. Zhitomirsky, R. Debnath, L. Levina, L. R. Rollny, G. H. Carey, A. Fischer, K. W. Kemp, I. J. Kramer, Z. Ning, A. J. Labelle, K. W. Chou, A. Amassian, E. H. Sargent, *Nat. Nano.* **2012**, *7*, 577.

Figures:

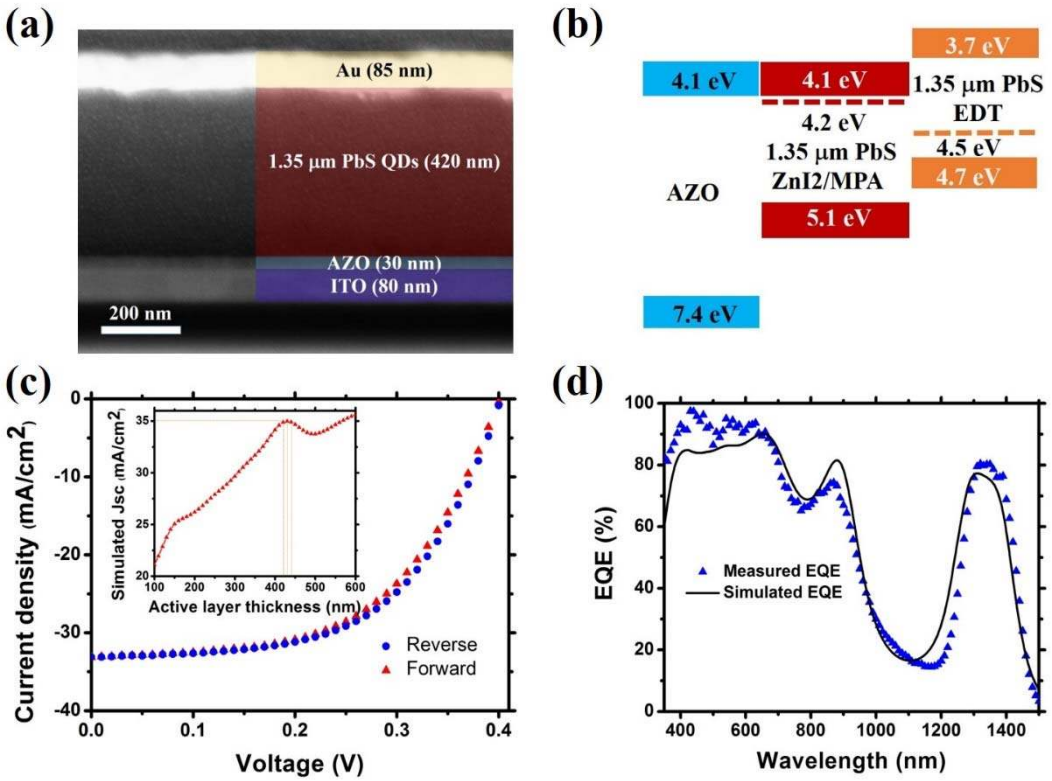

Figure 1. Characterizations of the optimized ZnI_2_MPA treated PbS solar cells: (a) FIB cross section image of the device structure, (b) the energy level diagram of the PbS components referenced to the vacuum level, (Detailed UPS data shown in Figure S2) (c) current density – voltage measurements in a forward and reverse scan under AM1.5 simulated solar illumination. Inset: simulated J_{sc} corresponding to varied active layer thickness with the device structure of ITO (90nm)/AZO (30nm)/PbS(100-600nm)/Au (80nm) and its corresponding. (d) Measured EQE curve and simulated EQE curve using TMM analysis.

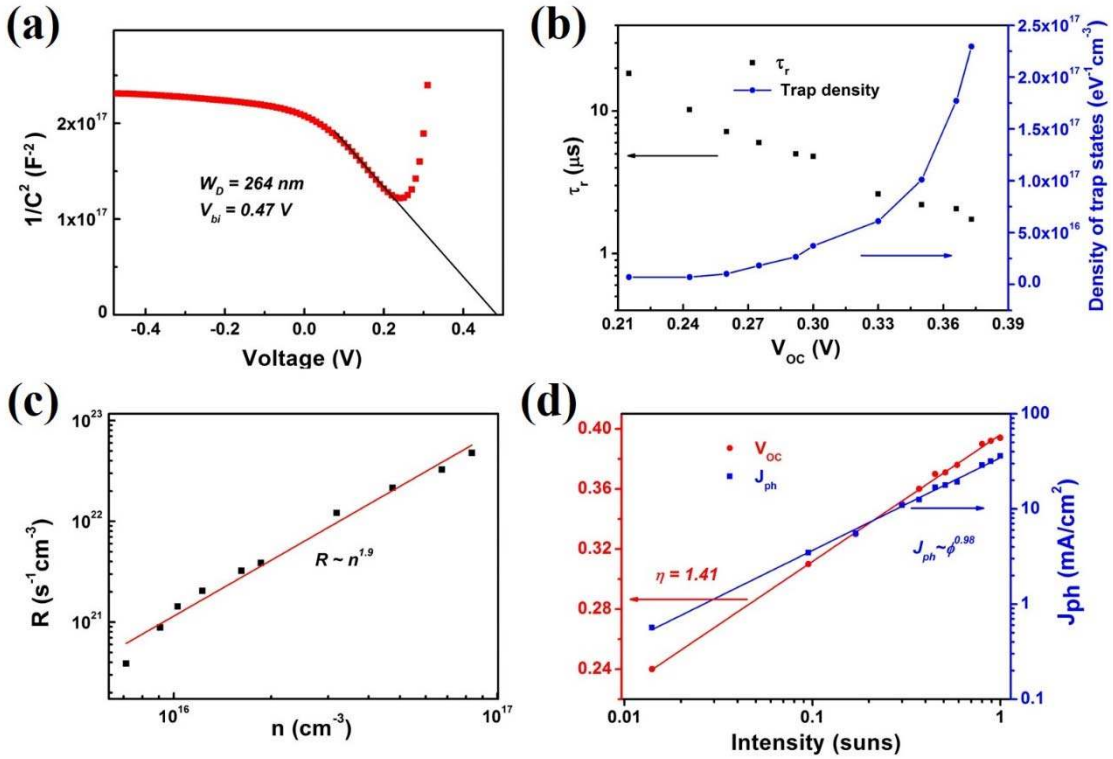

Figure 2. (a) Mott-Schottky analysis for calculation of the built-in potential and depletion width, determined from capacitance-voltage measurements of the typical IR PbS QDs device, TPV and TPC analysis: (b) Recombination lifetime (τ_r) and density of trap states as function of V_{OC} and (c) Recombination rate as a function of photogenerated charge carrier density, (d) Light intensity dependent V_{OC} and current density.

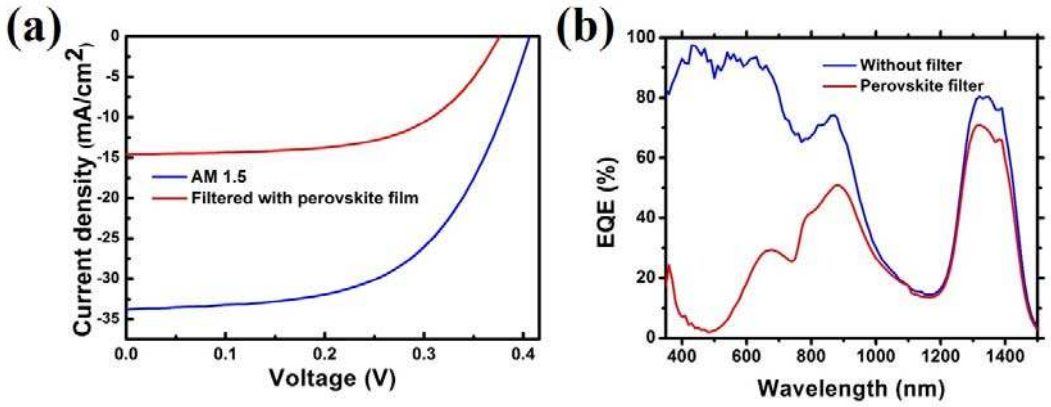

Figure 3. (a). Current density – voltage measurements under AM1.5 simulated solar illumination with and without using a perovskite filter (long pass 750nm) in front of the SWIR PbS QD solar cell; and (b) their corresponding EQE spectra.

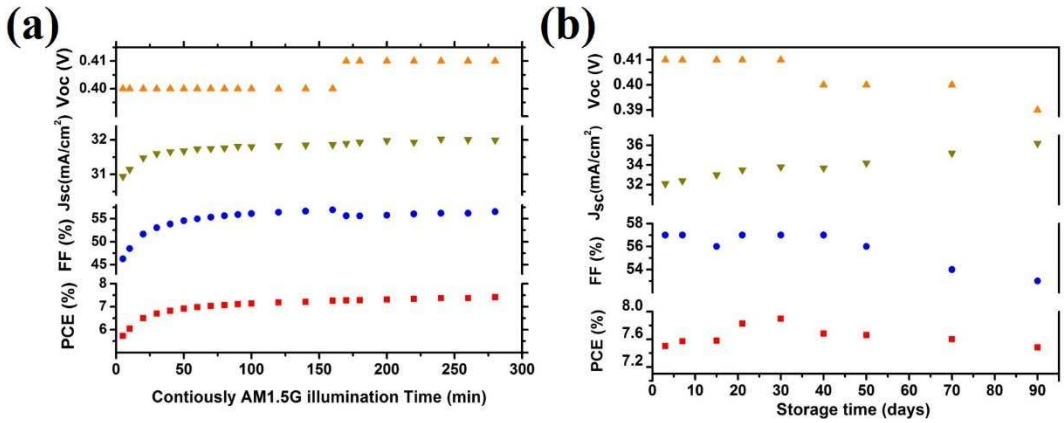

Figure 4. (a) Photostability measurements under continuous AM 1.5 simulated solar illumination in air with non-encapsulated device, (b) Long term stability test of a non-encapsulated device stored in ambient air conditions.

Tables:

Table 1. Different ligand exchange effects on 1.35 μm PbS QDs solar cells.

Device structures	V_{OC} [V]	J_{SC} [mA/cm^2]	FF [%]	PCE [%]
AZO/ 12layer ZnI2_MPA +2layer EDT PbS/Au	0.43	26.6	59	6.71
AZO/ 12layer EMII +2layer EDT PbS/Au	0.36	11.77	26	1.12

Table 2. Device performance summary under AM1.5 solar simulator, perovskite filter and Si filters

Variation of filters	V_{OC} [V]	J_{SC} [mA/cm^2]	FF [%]	PCE [%]
Without filter	0.41	33.8	57	7.89
Perovskite filter	0.38	14.6	60	3.33
Si filter	0.32	3.44	61	0.67